Assessment of Different SPIV Processing Methods for an Application to Near-Wall Turbulence

Jie Lin, Jean-Marc Foucaut, Jean-Philippe Laval, Nicolas Pérenne, and Michel Stanislas

Laboratoire de Mécanique de Lille (LML, UMR 8107),
Boul. P. Langevin, 59655 Villeneuve d'Ascq, France
michel.stanislas@ec-lille.fr

Abstract. An experiment has been performed in a large wind tunnel with the objectives to record 2D3C velocity fields of a fully developed turbulent boundary layer along a flat plate by means of stereoscopic PIV (SPIV) and to study the characteristics of this turbulence. The present study starts from determining the suitable method to process the database that was recorded with the stereoscopic PIV system. It suggests that the Soloff method with 3 calibration planes and integer shift is the best choice. Then, by using this method the analysis of the mean streamwise velocity, velocity fluctuations, Reynolds shear stress, spectrum, probability density function (PDF) as well as skewness and flatness, was performed and compared with values from hot-wire anemometry (HWA) and direct numerical simulation (DNS). The comparison indicates that SPIV is a well-qualified method to investigate near-wall turbulence.

1 Introduction

PIV is a quantitative, nonintrusive method for the measurement of fluid velocity in large areas. For the last 15 years, due to the strong improvement of laser, video camera and computer, PIV has undergone major developments and has become a powerful technique to investigate fluid mechanics [1–4]. The conventional implementation of PIV uses only one camera to record the motion of small tracer particles in a thin lightsheet. By using such a configuration, only two inplane components of the fluid velocity can be obtained in the plane of observation. The two components provide a wealth of information for many flows, however, it is sometimes rather difficult to understand the true physical significance of the observed flow phenomena without the third component. This is particularly true in turbulence. Therefore, it is necessary to measure all three components of the velocity in order to understand the organization of flow. Moreover, the out-of-plane component can introduce errors due to the optical projection [5]. Stereoscopic PIV have been developed to resolve these problems [6]. In SPIV, a stereoscopic camera system is used, in which the motion of the tracer particles is viewed from two different directions. Due to the out-of-plane motion, the two cameras see the tracer

A. Schroeder, C. E. Willert (Eds.): Particle Image Velocimetry,
Topics Appl. Physics **112**, 191–221 (2008)

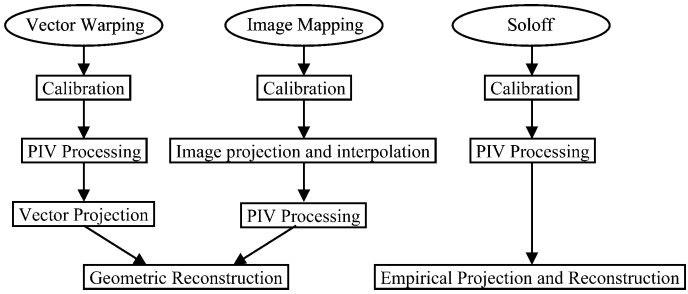

Fig. 1. Flowchart of vector warping, image mapping and Soloff method

particles travel over slightly different distances. From the differences in the apparent inplane motion it is possible to reconstruct all three components of the displacement. In the past decade, this method has been well developed and applied by a number of researchers [6–10]. It has been shown that the SPIV method can reach as good an accuracy as standard PIV [11]. However, the assessment of turbulence statistics with this technique has not been characterized in detail. In this chapter, the details of different methods for processing SPIV images are discussed and applied to near-wall turbulence.

The chapter proceeds as follows: Sect. 2 reviews and describes briefly the theory of stereoscopic-PIV algorithms. It is followed by a presentation of the experimental facility and setup in Sect. 3. In Sects. 4 and 5, SPIV processing is carried out in order to compare different algorithms and to select the most suitable one for the present database. Section 6 presents the turbulent statistics of the database using the selected algorithm and compares the results with those from hot-wire anemometry and numerical simulations. Section 7 finally concludes the present contribution.

2 Stereoscopic PIV Algorithms

Beside the standard pinhole model, recently discussed by *Wieneke* [12], which was not tested in the present study, three main algorithms are presently available to process SPIV images: vector warping [10], image mapping [10] and the Soloff technique [7]. These three methods are detailed in [11] and are summarized in the flowchart in Fig. 1.

2.1 Vector-Warping and Image-Mapping Methods

2.1.1 Empirical Backprojection

To process SPIV measurements, one needs to build an accurate relationship between the image plane of each camera and the object space. This is referred to as backprojection. The function for this relationship is usually generated

empirically by using a calibration grid. It allows us to map each point of the image plane onto the corresponding point in the object space, which corresponds to the measurement point. The perspective backprojection function was proposed by *Raffel* et al. [3] as a ratio of second-order polynomials. In general, a least-squares fit between a large number of couples (object-image points) is used to determine the coefficients of this function. Except for the variations in the analytical form, this procedure is considered as standard. Recently, *Fei* and *Merzkirch* [13] proposed a third-order polynomial function in order to increase the accuracy of this projection. In the present study, a ratio of second-order polynomials was chosen [3]. This polynomial method allows us to take into account some optical distortion. In addition to its higher order (at least equivalent to fourth order), the ratio of polynomial function is based on an analytical projection function that takes into account the perspective effect of the Scheimpflug deformations. Both vector warping and image mapping use the empirical backprojection to project the vectors and images, respectively, into the object space. Both methods use the geometric reconstruction to obtain the 2D3C velocity fields [8]. However, the procedures of the two methods are different and described in detail below.

2.1.2 Vector Warping

A uniform mesh is firstly generated in the object plane and projected to obtain a deformed mesh in each camera image plane. This eliminates the need for any vector interpolation processing during the reconstruction process. On each point of the deformed mesh, the 2D2C-vector field is then calculated by using a standard PIV processing for each camera. After this processing the two vector fields are backprojected into the object space. The velocity vectors of each camera are referenced at the same point of the initial uniform mesh. Finally, a geometrical reconstruction method is applied to obtain a 2D3C-vector field from the 2D2C-vector fields from each camera (1–2):

$$\begin{aligned} U &= \frac{U_1 \tan\alpha_2 - U_2 \tan\alpha_1}{\tan\alpha_2 - \tan\alpha_1} \\ V &= \frac{U_2 - U_1}{\tan\alpha_2 - \tan\alpha_1} \\ W &= \frac{1}{2}\left(W1 + W2 + (U_2 - U_1)\frac{\tan\beta_1 - \tan\beta_2}{\tan\alpha_1 - \tan\alpha_2} \right), \end{aligned} \tag{1}$$

with

$$\begin{aligned} \tan\alpha_1 &= \frac{X_1 - x}{y - Y_1} \qquad & \alpha_1 &= \frac{X_2 - x}{y - Y_2} \\ \tan\beta_1 &= \frac{Z_1 - x}{y - Y_1} \qquad & \tan\beta_1 &= \frac{Z_2 - x}{y - Y_2}\,. \end{aligned} \tag{2}$$

The coordinate system for reconstruction is presented in Fig. 2. U, V and W are the resulting three velocity components after reconstruction along

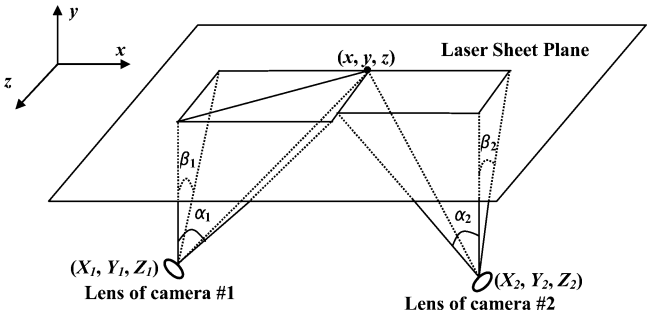

Fig. 2. Reconstruction in a stereoscopic PIV configuration

the X, Y and Z coordinates axis, respectively, while U_1 and W_1 refer to the two inplane components obtained by 2D2C analysis from camera #1, U_2 and W_2 are obtained from camera #2. (X_1, Y_1, Z_1) and (X_2, Y_2, Z_2) are the positions of the lenses of camera #1 and camera #2, respectively, in the object space, while (x, y, z) is the position of the measurement point.

2.1.3 Image Mapping

The recorded PIV images are firstly backprojected, or "mapped", to the object space pixel by pixel and interpolated on a new regular grid. The fields of 2D2C vectors are then calculated directly from these images by using standard PIV processing on a common regular grid. Subsequently, the geometric reconstruction method is used to obtain a 2D3C-vector field from two 2D2C-vector fields as with the vector warping method. The same reconstruction process is used for both methods. It should be mentioned that for both image mapping and vector warping, the geometrical reconstruction needs the value of some geometrical parameters (such as the position of the lens, see (2)), which are difficult to measure accurately on the experimental setup.

2.2 Soloff Method

Optical distortion due to inaccurate optical alignment, lens nonlinearity, refraction by optical windows, fluid interfaces and other optical elements of an experiment can generate inaccuracy by introducing spatial variations of magnification. It is important to compensate for these distortions because fractional changes in the magnification have a one-to-one effect on the accuracy of the measured velocity. *Soloff* et al. [7] introduced a general empirical calibration procedure, which allows us to obtain a specific matrix of the distorted imaging system, and an algorithm to accurately compute the velocity fields from measurements of distorted PIV images. From the calibration that is made by recording several images of a target, *Soloff* et al. [7] proposed

to optimize a mathematical formalism that combines the projection and the reconstruction (3).

$$\begin{Bmatrix} \overline{\Delta X_1^1} \\ \overline{\Delta X_2^1} \\ \overline{\Delta X_1^2} \\ \overline{\Delta X_2^2} \end{Bmatrix} = \begin{Bmatrix} F_{1,1}^1 & F_{1,2}^1 & F_{1,3}^1 \\ F_{2,1}^1 & F_{2,2}^1 & F_{2,3}^1 \\ F_{1,1}^2 & F_{1,2}^2 & F_{1,3}^2 \\ F_{2,1}^2 & F_{2,2}^2 & F_{2,3}^2 \end{Bmatrix} \begin{Bmatrix} \overline{\Delta x_1} \\ \overline{\Delta x_2} \\ \overline{\Delta x_3} \end{Bmatrix} . \tag{3}$$

Here, the superscripts 1 and 2 indicate the camera #1 and #2, respectively. $\overline{\Delta X}$ is the displacement in the image plane (two dimensions) and $\overline{\Delta x}$ is the displacement in the object plane (three dimensions). F refers to the corresponding mapping function. The subscripts 1 and 2 represent the two inplane displacements, while the subscripts 3 stand for the out-of-plane displacement. The Soloff method is based on a third-order polynomial function for the inplane components and a second-order one for the out-of-plane component. At least two target images (with an accurately known spacing) are necessary to calibrate the Soloff method. In this study, three or five target images were used.

2.3 Comparison of the Three Methods

The main difference among the three methods is that the Soloff technique uses empirical optical projection and reconstruction, while vector warping and image mapping use empirical optical projection but geometrical reconstruction. Considering vector warping and image mapping only, vector warping projects the vectors and image mapping interpolates images. The drawback of the warping or Soloff methods is that the PIV analysis is conducted in the image plane, which leads to a local magnification that is not the same along the field. The interrogation window, which has a constant size in pixels in the image plane, then varies in size in the object space. On the contrary, the mapping method projects the images in the object space, making the magnification constant, but it distorts the particle images and introduces interpolation errors.

2.4 Calibration and Correction of Positions of the Image Planes

Calibration is a way to determine the relationship between the position in the object space and that in the image plane. For this purpose, it is necessary to acquire images of a calibration target whose location in the object space is known. By using these calibration targets, a generalized function to project the data from the image plane onto the object space can be found. According to the literature, a second-order polynomial [9] and a second-order ratio of polynomials [8] were used for a 2D calibration, while a cubic and a quadratic

polynomial [7] and bicubic splines [14] were developed for a 3D calibration. In an experiment, however, it is difficult to make the position of the lightsheet and the calibration plane exactly the same. There are always small offsets and tilts between calibration and measurement planes. *Coudert* and *Schön* [10] proposed a method to correct the offset and tilt between them. The method works as follows. A set of single-exposure PIV images from each camera recorded at the same time is firstly backprojected as in the mapping method. A standard PIV processing is then used to calculate the displacement fields of the particle images illuminated at the same time by the same laser pulse. If the measurement and the calibration planes are perfectly superimposed, the mean displacement is zero (computed from about 50 vector fields). Normally, one can observe a small displacement from which an offset and tilt between the calibration and measurement planes can be deduced. Following this, a correction procedure is carried out to improve the projection function.

3 Experimental Setup

3.1 Wind Tunnel

The experiment was carried out in a boundary-layer wind tunnel (see [15] for details on the wind tunnel). This wind tunnel is $1 \times 2\,\mathrm{m}^2$ in cross section and 21.6 m in length. In order to use optical methods, the last 5 m of the working section is transparent on all sides. An air-water heat exchanger is located in the plenum chamber to keep the temperature within $\pm 0.2\,^{\circ}\mathrm{C}$. The turbulent boundary layer is studied on the bottom wall of the wind-tunnel test section. This flow presents a tiny longitudinal pressure gradient that is negligible and has no effect on the near-wall turbulence. The Reynolds number based on the momentum thickness Re_θ can reach 20 600 with a boundary layer thickness δ of about 0.3 m. The external velocity in the testing zone of the wind tunnel can vary from 0 to 10 m/s with a stability better than 0.5 %.

3.2 SPIV Setup

The purpose of the experiment was to obtain 3C velocity fields in planes parallel to the wall of a boundary layer, as close as possible to the wall. A Nd:YAG pulsed laser, with 2×250 mJ of energy at 15 Hz, was used to generate the lightsheet. This lightsheet was shaped using a conventional optical setup (one sperical and one cylindrical lens) with a thickness of about 0.75 mm. The lightsheet passed through a lateral window located 1 m away from the measurement area. Two PCO SENSICAM cameras (1280×1024 pixel^2) were positioned under the wind tunnel as shown in Fig. 3. The cameras were arranged so that the Scheimpflug condition [8] was satisfied. The H and L parameters defined in Fig. 3 are: $H \cong 52$ cm and $L \cong 50$ cm. These distances, which are necessary for the geometrical reconstruction, are measured with

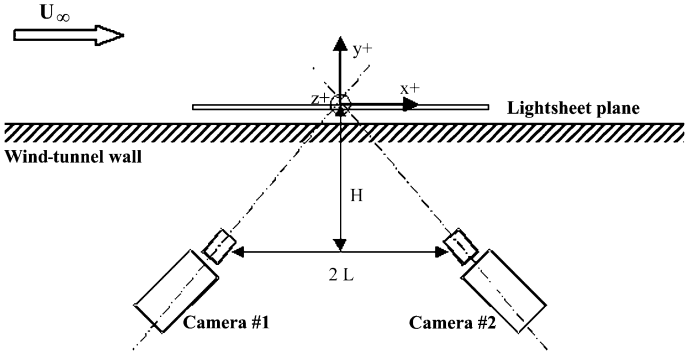

Fig. 3. Setup of the experiment and frame of reference for data analysis

respect to the center of the field of view. The line joining the two cameras is parallel to the main flow (camera #1 being upstream). The flow is from left to right in the images delivered by both cameras. The lightsheet propagates in the test section along z. Both cameras stand on the same ground under the wind tunnel upstream and downstream of the lightsheet in order to obtain symmetric light-scattering conditions. The focal length of the camera lenses was 105 mm. The field of view extends over $6.5 \times 4.0\,\mathrm{cm}^2$ and $f_{\#} = 5.6$ was used for both cameras during the experiments. The average magnification is approximately 50 m/pixel in the object space. The depth of field was 3.5 mm. The focus was set at the middle value of the explored y domain and kept there for the remainder of the experiment (including the acquisition of calibration images). In this configuration, the Airy disk diameter is about 8.2 μm, which gives a size of the order of 1.3 pixels [1]. In order to measure this size more precisely, the autocorrelation of a single image was calculated. From the correlation result, the particle image size at 2σ is about 1.5 pixels and 1.3 pixels in streamwise and spanwise directions, respectively. This slight anisotropy is attributed to the stereoscopic distortion. The experiments were performed at $U = 3\,\mathrm{m/s}$ (free-stream velocity). With this velocity, the Reynolds number Re_θ, based on the momentum thickness, is 7800. The friction velocity u_τ is of the order of 0.12 m/s. A wall unit ($\Delta y^+ = 1$) is 0.125 mm. Ten planes parallel to the wall were characterized. A total of 500 image pairs in each plane were recorded for each camera. The first plane was placed as near as possible to the wall, while avoiding too many reflections. The spacing between two neighboring planes was about 4 wall units.

4 Stereoscopic PIV Processing

As mentioned above, various methods including image mapping, vector warping and Soloff are available to obtain 2D3C results from SPIV. For each method, there are also several different choices of tools or parameters. There-

Table 1. Methods description

Short name	Method	Specialty	Shift method
MSI	image mapping	surfacial interpolation	integer shift
MSW	image mapping	surfacial interpolation	Whittaker shift
MWI	image mapping	Whittaker interpolation	integer shift
MWW	Image mapping	Whittaker interpolation	Whittaker shift
S3I	Soloff	3 calibration planes	integer shift
S3W	Soloff	3 calibration planes	Whittaker shift
S5I	Soloff	5 calibration planes	integer shift
S5W	Soloff	5 calibration planes	Whittaker shift
WI	vector warping		integer shift
WW	vector warping		Whittaker shift

fore, it is necessary to select one method with the best set of parameters for computation. In this section, the image number 10 of plane 5 was used in the first step to make a comparison of the instantaneous velocity fields provided by the different processing choices. Then, a statistical comparison was conducted using PDFs and spectra computed on the first 100 images of the plane 5.

The following methods were compared: image mapping with surfacial [16] or Whittaker [17] method to interpolate the image, vector warping and Soloff. For each method, the PIV analysis was performed with integer and subpixel Whittaker shift. In the case of Soloff, 3 and 5 calibration planes were taken. Table 1 shows the details of the methods and their abbreviations used in this chapter. For all the methods, a three-step multigrid approach was employed (window sizes: 64×64, 32×32 and 32×32 pixel^2).

As described earlier, calibration and its correction should be carried out before PIV processing. In the present study, 60 pairs of the first images of camera #1 and camera #2 are sufficient to calculate the average offset and tilt between calibration and measurement planes with a good convergence. By taking this value into account, the projection functions were corrected and the real position of the lightsheet was determined (see Table 2). Figure 4 shows the misalignment error between calibration plane 7 and laser plane 5 as an example. The vectors in Fig. 4 are quite constant, which means that the calibration and measurement planes are nearly parallel. The mean displacement in Fig. 4 is 0.58 mm, which implies a separation between calibration plane 7 and laser plane 5 of about 0.29 mm in depth (as the Scheimpflug conditions was used). This distance is taken into account in the correction process [10]. The gain in accuracy provided by the correction will be discussed further downstream.

In order to select suitable calibration plane(s) for each method, the location of each calibration and laser plane are listed in Table 2. Laser plane 5 is considered as an example. Based on Table 2, calibration plane 7 was used for image mapping and vector warping, calibration planes 6, 7, 8 were used

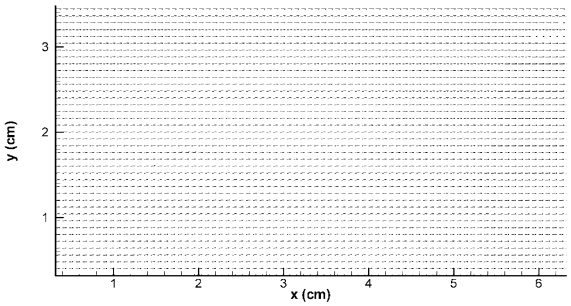

Fig. 4. Offset and tilt between calibration (No. 7) and measurement planes (plane 5)

Table 2. Absolute positions of the calibration and measurement levels

#	Calibration position (mm)	Laser position (mm)	Laser position (wall unit)	Dt (s)
1	0.68	1.81	14.5	600
2	1.15	2.32	18.5	600
3	1.61	2.78	22.2	400
4	2.07	3.29	26.3	400
5	**2.53**	**3.71**	29.7	350
6	**2.99**	4.16	33.3	350
7	**3.42**	4.63	37	350
8	**3.91**	5.07	40.6	350
9	**4.37**	5.5	44	300
10	4.83	5.99	48	300
11	5.29			

for the Soloff method with 3 calibration planes and calibration planes 5, 6, 7, 8, 9 were used for the Soloff method with 5 calibration planes. Table 2 also gives the PIV time delay for each plane, which was optimized to give a mean displacement of the order of 10 pixels in each field.

The comparison starts by comparing the accuracy of computation of the different methods. As the exact result is unknown, only relative comparisons between the different methods are possible. For this purpose, the following two error estimations were computed:

– Mean value of the modulus:

$$E_1 = \frac{\sum_{i=1}^{N} \sqrt{(u_1^i - u_2^i)^2 + (v_1^i - v_2^i)^2 + (w_1^i - w_2^i)^2}}{N} . \quad (4)$$

Table 3. Accuracy of the different methods

# line	Reference	Comparing with	E_1 (pixel)	E_2 (pixel)
1	WI	WW	0.12	0.35
2	S3I	S3W	0.11	0.22
3	MSI	MSW	0.09	0.58
4	MWI	MWW	0.11	0.59
5	MSI	MWI	0.15	0.61
6	MSW	MWW	0.18	0.6
7	MWI	MSW	0.17	0.59
8	S3I	S5I	0.04	0.26
9	MSI	WI	0.59	0.7
10	WI	S3I	0.13	0.63
11	MSI	S3I	0.75	0.67

– Standard deviation of the modulus:

$$E_2 = \sqrt{\frac{\sum_{i=1}^{N} \left(\sqrt{(u_1^i - u_2^i)^2 + (v_1^i - v_2^i)^2 + (w_1^i - w_2^i)^2} - E_1\right)^2}{N-1}}. \quad (5)$$

Here, (u_1, v_1, w_1) and (u_2, v_2, w_2) are the three instantaneous velocity components for, respectively, the reference and compared method. N is the total number of velocity vectors in the field. The values of E_1 and E_2 for the different methods are presented in Table 3.

Table 3 shows that the differences of the two parameters E_1 and E_2 between integer shift and Whittaker (subpixel shift) are quite small for both vector warping (line 1) and Soloff methods (line 2). This can be explained by the fact that the Whittaker shift, which is expected to reduce the peak locking, does not show any strong improvement from a statistical point of view [18]. The peak-locking effect appears mainly on the PDF of the velocity. This will be discussed in the next paragraph. As far as the image-mapping method is concerned, the comparison between two different shifts (line 3 and 4) gives a smaller value of E_1 than the comparison of two different interpolation methods (line 5 and 6). The values of E_2 of lines 3 and 4 keep the same order of magnitude but are generally two times higher than those with vector warping or Soloff methods (line 1 or 2). This suggests that both interpolation and shift methods have a strong influence on image mapping. Clearly, several successive interpolations (i.e., MWW or MSW) can damage the shape of the particle images and thus the correlation peak. However, it would be possible to couple both interpolations necessary for the projection and the subpixel shifting at the same step. The fact of using only one interpolation for both operations should improve the accuracy but will increase the computational time (interpolation is necessary at each pass of computation). As shown in line 8 of Table 3, the results of the Soloff method with 3 calibration planes and 5 calibration planes are similar to each other. This implies

that, in the present configuration (lightsheet thickness, low distortion), it is not necessary to use 5 planes to calibrate the Soloff method. The comparison between MSI and WI in line 9 shows high values of both E_1 and E_2. These are introduced by the projection of images and strong differences are evident in the results. The comparison between vector warping and the Soloff methods (line 10) shows a small value of E_1 and a large value of E_2. The difference between Soloff and vector warping can only be attributed to the reconstruction that decreases the noise effect in the case of Soloff. This is confirmed by the comparison between MSI and S3I (line 11), which shows high values of E_2 but also of E_1. Besides the influence of the projection of images already evidenced in line 9, the reconstruction is the other source of this difference.

As shown in Table 3, the effect of subpixel shift is not evidenced by the comparison of lines 1 to 4. The reconstruction probably has a filtering effect, which decreases the peak locking. Therefore, the histogram of the decimal part of the velocity, in pixels, is calculated to analyze the effect of this peak locking. Figure 5 compares the histogram of the 2D2C PIV analysis (before reconstruction) for cameras #1 and #2 (C1 and C2) in the case of Soloff methods: S3I and S3W. *Foucaut* et al. [18] show a strong improvement when Whittaker interpolation is used for subpixel shifting. In the present case, this improvement is less visible, probably due to a particle image diameter smaller than two pixels [18]. Even if the Whittaker interpolation is used, a small peak-locking effect can still be shown for the u-component (u_{2C}). This effect is still larger for the w-component (w_{2C}). Figure 6 shows the histogram of the decimal part of the velocity after reconstruction by the Soloff method for the out-of-plane component v (which behaves like the u-component) and for the spanwise component w (less affected by the stretching of the SPIV). Due to the perspective effect of SPIV, a mean magnification was used to convert physical units to pixels. It is clear that the peak locking is filtered and that S3I and S3W give essentially the same histogram for both components presented in Fig. 6. Only some small oscillations remain due to a combination of peak locking, projection (variation of magnification along x) and reconstruction (between both 2D2C fields). To analyze the effect of these oscillations, the PDF of the velocity fluctuations can be studied. Furthermore, to characterize the measurement noise level, it is also interesting to look at the influence of the processing algorithm on the spectrum [4] of the velocity fluctuations. For this purpose, the S3I, S3W, MWI and WI methods were selected from the previous analysis to process 100 images pairs, which were used to obtain the spectrum and PDF of the three velocity components.

The components u and v are computed from U_1 and U_2 (1). As the angle of view is close to 45° in the present experiment, the behavior of these two components is similar. The w-component is perpendicular to the plane of the cameras and it is thus less affected by the stereoscopic reconstruction. Therefore, all the results of the spectrum and PDF are presented only for the components v and w. In Fig. 7, E_{22} and E_{33} are spectra of the v- and

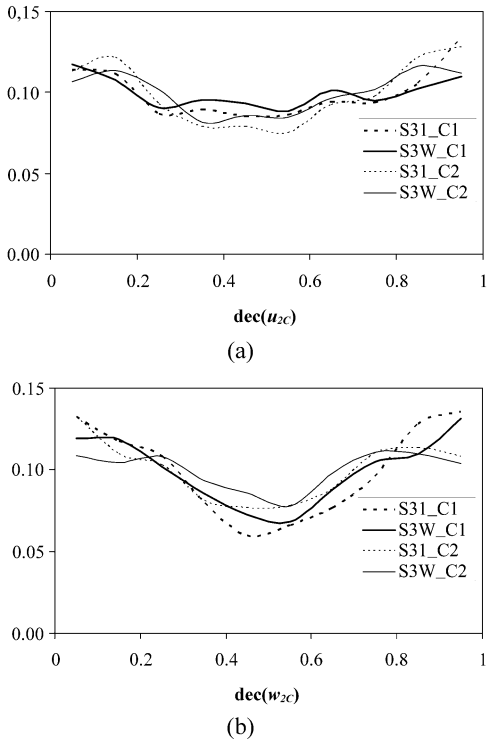

Fig. 5. Decimal part histogram of the u-(**a**) and w-(**b**) components of each camera before projection and reconstruction

w-components, respectively, and k is the wave number. According to the theory of *Foucaut* et al. [4], k_c is the PIV cutoff wave number ($k_c = 2.8/S_{IW}$, where S_{IW} is the interrogation window size). The PIV results are qualified only in the region $k \leq k_c$. Figure 7 shows that the results of the four selected methods are almost the same in the valid region of PIV. The noise level, that is attained by the spectrum in the high-frequency part, is very close for each method. As in 2D2C PIV [18], a subpixel shift does not improve the spectrum as compared to the integer shift. This means that from the spectral point of view, all these methods can be used.

In Fig. 8, the PDFs of WI, S3I and S3W are very similar but MWI seems rather different from the others. The differences cannot be attributed to the reconstruction because image mapping and vector warping use the same reconstruction process. They may arise from the fact that the image-mapping method interpolates the deformed images before PIV processing, whereas the vector warping and Soloff methods are performed directly on the CCD images. As explained before, the perspective effect generates a difference in physical window size along the field and thus introduces a kind of smoothing

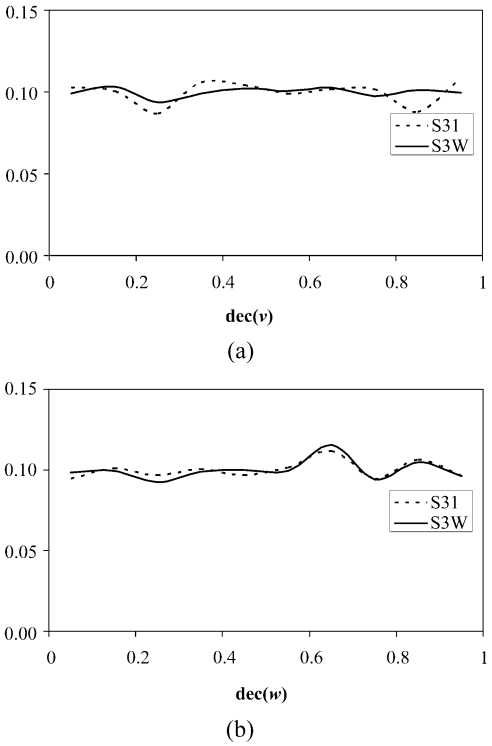

Fig. 6. Decimal part histogram of the v-(**a**) and w-(**b**) components after projection and reconstruction

in the statistics. This effect is clearly visible in Fig. 8a, as in Fig. 5. Moreover, the image-mapping method makes the magnification constant. As a consequence, particle images that are slightly affected by the interpolation are now deformed. This probably induces the modification of the peak locking that appears in Fig. 8b. The method S3W using the Whittaker subpixel shift does not efficiently remove the peak locking. Figures 9a–c show the PDF in pixels of the 3 components for three planes, plane 1 ($y^+ = 14.5$) is closest to the wall and plane 10 ($y^+ = 48.0$) is the furthest. Some fluctuations similar to peak locking are clearly visible in Figs. 9a and c. However, the fluctuations do not appear in Fig. 9b because the out-of-plane component presents a smaller dynamic range. They are probably smoothed out in this case. In Fig. 9a, the result of plane 1 shows different behavior from plane 5 and plane 10. This difference mainly arises from the fact that the dynamic range and the ratio of this range to the mean velocity of the u-component, is very large in this position, which causes the large range of the oscillations. Besides, the large velocity gradient at this position also has some influence. In Fig. 9c, small peaks can be found in the PDF of plane 1, which results mainly from

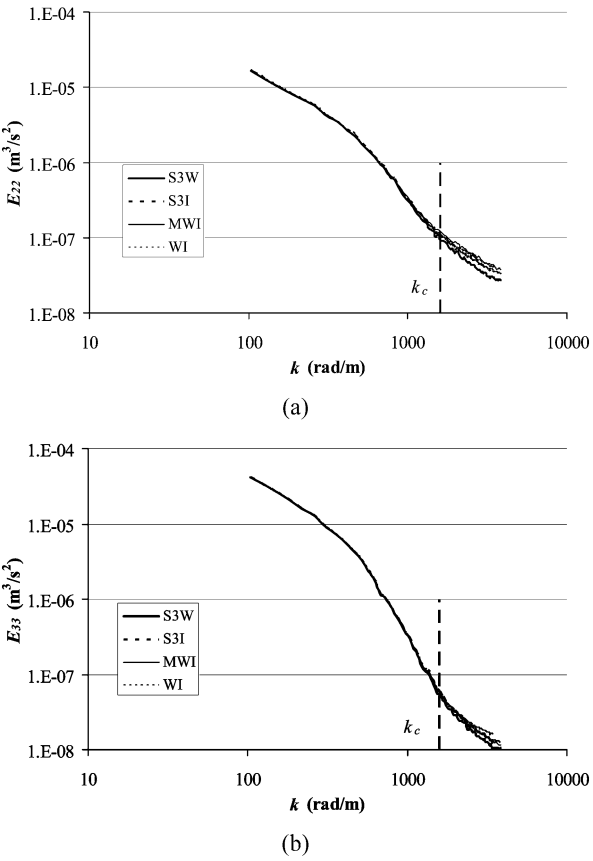

Fig. 7. Comparison of the velocity spectrum of the v-(**a**) and w-(**b**) components for different methods

the large velocity gradient at this position. The reduced amplitude of the peak locking benefits from the decrease of the velocity gradient away for the wall. Furthermore, the periodic distance of the main peaks is equal for all three planes, which implies a nearly constant dynamic range of the velocity fluctuation w'.

To study the magnitude of the velocity gradient and its variation with the wall distance, Fig. 10 shows the difference of particle displacement normalized by the particle image size between the top and the bottom of the lightsheet that has a thickness of about 0.75 mm [18, 19]. In 2D2C PIV, the criterion proposed by these authors to minimize the effect of gradient is $Du/di < 0.5$. In the present experiment, this parameter, computed from the mean gradient using the Van-Driest model [20], decreases as the distance to the wall increases and it seems acceptable when reaching plane 4. But there are still oscillations

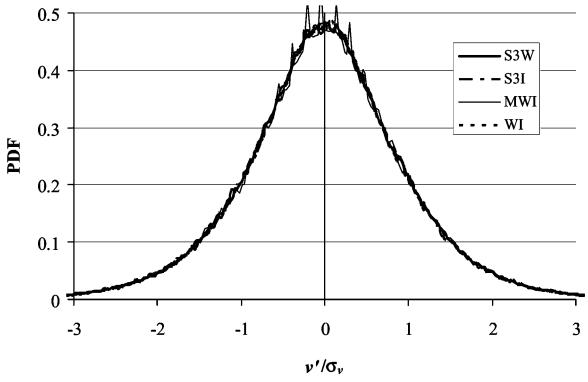

(a)

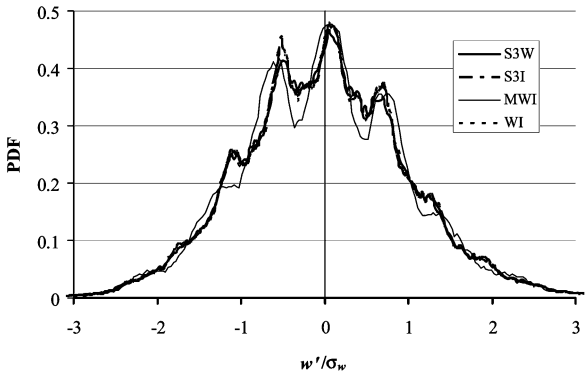

(b)

Fig. 8. Comparison of the PDF of the normalized fluctuations of the v-(**a**) and w-(**b**) components for different methods

of the PDF in this plane. This is probably due to the fluctuation of the instantaneous velocity gradient around this mean value and to a residual peak locking due to the particle image size (about 1.4 pixels).

The time needed by the different methods was computed and is listed in Table 4. It is estimated from a computation on a small sample of images (based on a computer with a PIII 800 processor and 256M RAM). The methods with Whittaker shift take the longest time for computation, about 4 times longer than the rest. For the image-mapping method, Whittaker interpolation needs much more time than surfacial interpolation when the computation is carried out with the same shift method.

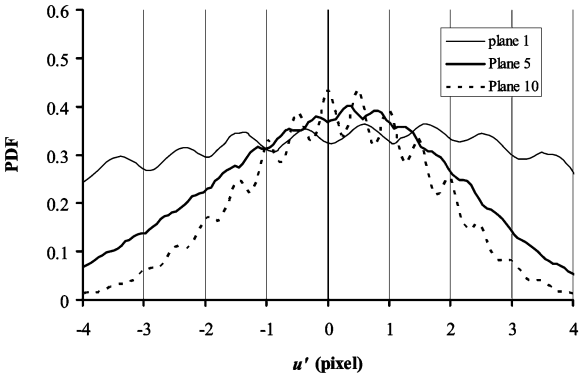

(a)

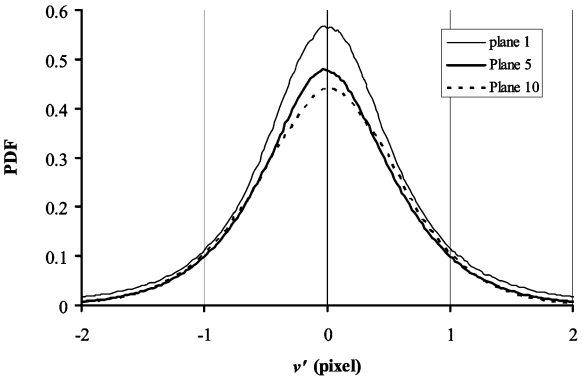

(b)

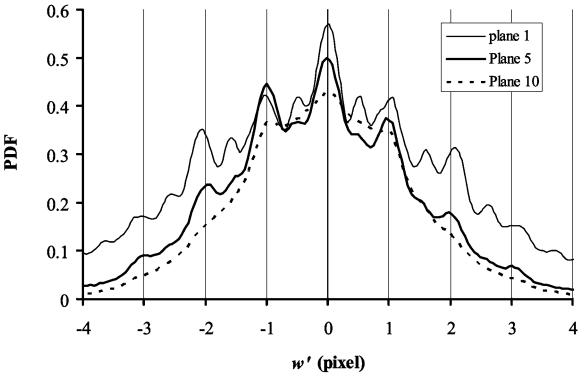

(c)

Fig. 9. PDF of the fluctuations of the u-(**a**), v-(**b**) and w-(**c**) components for different planes

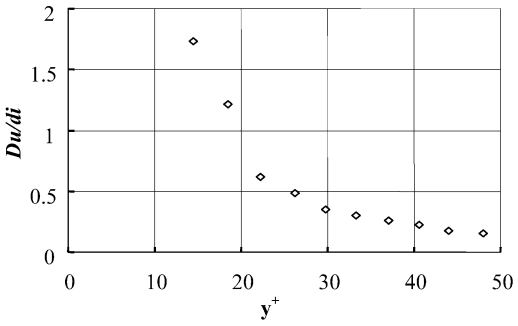

Fig. 10. Difference of velocity between the top and the bottom of the lightsheet for different wall distances

Table 4. Time consumption of the different methods for 500 image pairs

Method	MSI	MSW	MWI	MWW	S3I	S3W	S5I	S5 W	WI	WW
Time (h)	20	100	50	130	20	110	20	110	25	110

5 Method Selection

Based on the above results, the following arguments can be put forward:

Regarding the image-mapping method, the procedure of image interpolation can introduce errors that are impossible to avoid. A proper interpolation method such as Whittaker reduces the errors and thus improves the accuracy of the results. In addition, for window shifting, Whittaker is a subpixel shift that in principle is more accurate than the integer shift. As discussed before, the image-mapping method using Whittaker interpolation and Whittaker shift cannot be used together because two successive interpolations affect the correlation peak shape. Therefore, the most accurate method should retain Whittaker interpolation only once: for the image mapping or for the window shifting. However, it needs much more computational time in both cases compared to other interpolation techniques. Focusing on the PDFs in Fig. 8, it is clear that the mapping method causes more peak locking than the methods based on vector projection.

With respect to the vector warping method, when Whittaker shift is used, the computation is heavier and the accuracy of the results does not improve much. Therefore, to save computer time it is recommended to use integer shift when the vector warping method is selected.

As for the Soloff method, Table 3 shows that the Soloff with 5 calibration planes and with 3 calibration planes give very similar results. Therefore, it is not necessary to use 5 calibration planes. Additionally, the difference between the Whittaker and integer shifts is so small that the Whittaker shift is useless in view of the extra computation effort. Consequently, the Soloff method with

3 calibration planes and integer shift appears as the best compromise when the Soloff method is considered.

When using image-mapping and vector warping methods, it is required to measure geometric parameters such as the angle of the camera and the distances between the optical centers of camera lenses and calibration planes. The errors on the measurement of these parameters will affect the result of both methods. For the Soloff method, these parameters are not required. In this regard, the Soloff technique avoids these measurement errors and thus possibly provides more accurate results. *Fei* and *Merzkirch* [13] found a method for determining the viewing direction in the ángular displacement stereoscopic system by means of a digital imaging procedure. The method appears to improve the accuracy of results by avoiding the direct measurement of geometrical parameters of the setup. They found that their results are quite similar to that of the Soloff method, which supports the reliability of the Soloff approach.

It should be noted that Whittaker shift can improve significantly the accuracy of the result when the particle image size is sufficient large (normally > 2 pixels). In the case of small particles, this shift method can hardly perform well. This is supported partly by the present results: almost no difference between integer and Whittaker shift, because the present particle image size is only about 1.4 pixels.

As a conclusion of this synthesis, it appears that the Soloff method with 3 calibration planes and an integer shift (S3I) is the best choice in the present state-of-the-art. It was thus used for the present analysis of all 10 planes. Using this method, the correction technique proposed by [10] could be studied. Figures 11 and 12 show the efficiency of this correction. The SPIV algorithm was applied to plane 5 using two different sets of calibration planes: (4 to 6) called N°5 expected when the experiment was done and (6 to 8) called N°7 that was selected according the result of correction (Table 2). As shown in Table 2, the calibration plane N°5 is shifted by about 1.2 mm from the lightsheet location N°5, while the calibration plane No. 7 is much closer. The results are computed with correction (noted C) or without correction (noted NC). Figure 11 illustrates the PDF of the v- and w-components in each case. When the correction is applied, the PDF is comparable whatever the calibration plane is. Figure 12 leads to the same conclusion from the spectrum. Table 5 presents the comparison of the parameters E_1 and E_2 (see (2)) for the correction. Line 1 shows a small difference between the results obtained with correction from the two calibration planes N°5 and No°7. If calibration plane N°7 is used without correction, the differences from the corrected results increase a little but stay acceptable (line 2). The small increases of E_1 and E_2 come from the distance of 0.3 mm (about 6 pixels) between the calibration plane N°7 and the measurement plane No. 5. In lines 3 and 4, when the calibration plane N°5 is used without correction the results are remarkably different from other combinations. Considering the fact that the correction

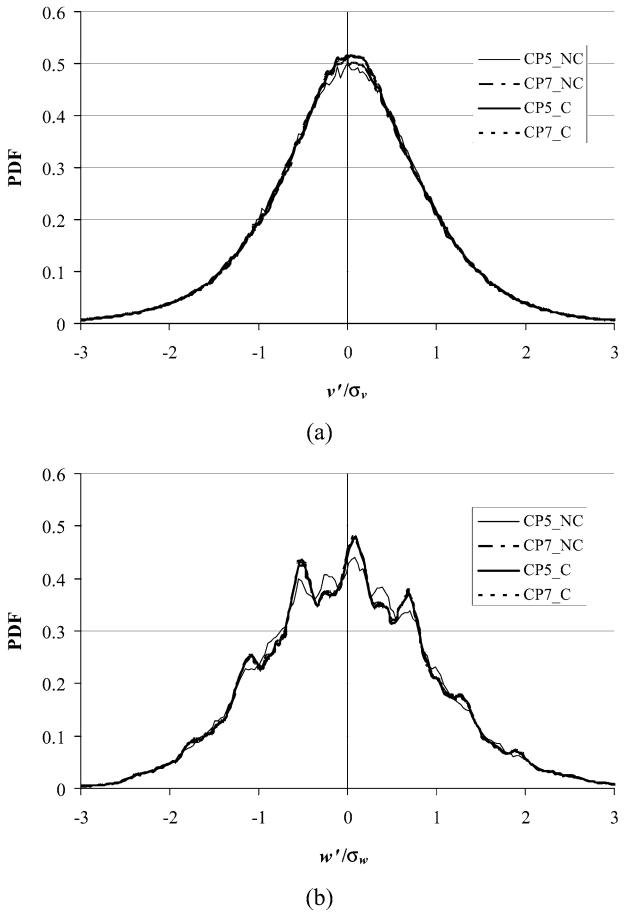

Fig. 11. Comparison of the PDF of the normalized fluctuations of the v-(**a**) and w-(**b**) components effect of correction

Table 5. Accuracy of the correction process

# line	Reference	Comparing with	E_1 (pixel)	E_2 (pixel)
1	CP7_C	CP5_C	0.11	0.4
2	CP7_NC	CP7_C	0.24	0.5
3	CP5_NC	CP5_C	0.66	0.63
4	CP5_NC	CP7_C	0.67	0.66

of calibration only takes a little time but can improve the accuracy of the results, correction is strongly recommended.

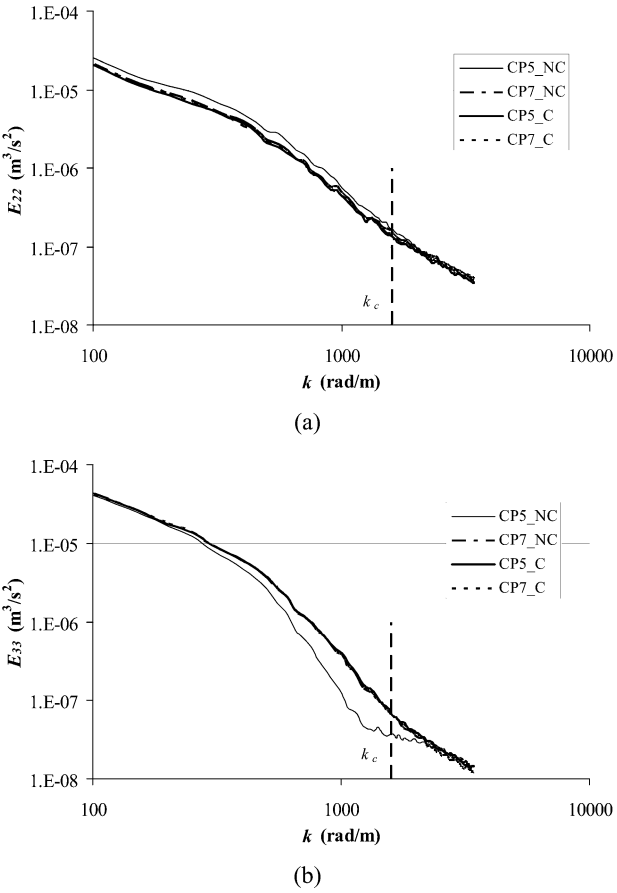

Fig. 12. Comparison of the spectrum of the v-(**a**) and w-(**b**) component effect of correction

6 Statistical Results for the 10 Planes

Using the selected S3I method with correction, the recorded SPIV images of the 10 planes were processed to obtain the instantaneous 2D3C velocity fields. In this process, three passes are used to calculate the standard 2D2C vector field. The window sizes are, respectively, 64×64, 32×32, and 32×32 (pixel^2) with a final spacing of 12 pixels (0.6 mm) corresponding to a mean overlapping of 67.5 %. Here, the 67.5 % overlapping is used to obtain better spatial resolution for detection of coherent structures in future work. The results were saved in a database built using the Pivnet 2 Netcdf format [21]. Then, a statistical analysis was performed to obtain the mean streamwise velocity and the Reynolds stresses, the velocity spectrum and PDF as well as skewness and flatness in the 10 planes. Here, these statistical results are

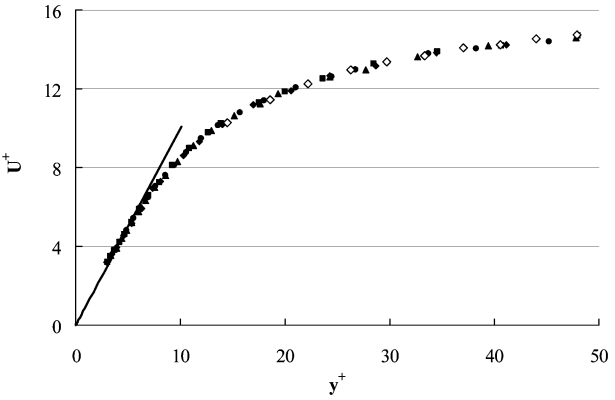

Fig. 13. Comparison of mean streamwise velocity distributions of SPIV (Re_θ = 11 400 (◊)) and hot-wire anemometry [15] (Re_θ = 11 400 (▲), 114 800 (■) and 20 600 (●))

compared with those of hot-wire anemometry [15]. Plane 4 was chosen to look at the spectra and PDF because it is in the middle of the range of wall distances studied ($y^+ = 26.3$) and it corresponds to the limit of validity for the velocity gradient inside the lightsheet (Fig. 10). In this section, the result that is normalized using the skin friction velocity u_τ ($= \sqrt{\tau_w/\rho}$, where ρ is the density of the fluid) and ν, is denoted with a superscript $+$.

Figure 13 shows the mean streamwise velocity profile in the near-wall region ($y^+ < 50$). In this figure the solid symbols correspond to hot-wire measurement [15] for different Reynolds numbers (Re_θ = 11 400 (▲), 14 800 (■) and 20 600 (●)). The hollow symbols correspond to the 10 planes measured with PIV. The straight line represents the viscous sublayer equation $u^+ = y^+$. This figure shows that the mean velocity obtained by SPIV is in perfect agreement with that of hot-wire anemometry.

Besides the mean streamwise velocity, the fluctuations of all three components are also basic characteristics of the turbulent boundary layer and thus need to be analyzed. Figure 14 shows a comparison of the profiles of the fluctuations obtained by the two methods (SPIV and HWA). These results are also compared with the results of the DNS by *Spalart* [22]. The Reynolds number of this simulation is $\mathrm{Re}_\theta = 1410$. The $\sqrt{\overline{v'^2}}$ profile is very similar for all the methods down to $y^+ = 15$. Below this value, no PIV measurements are available and the hot wire starts to show a wall interference due to the probe size. For $\sqrt{\overline{u'^2}}$ and $\sqrt{\overline{w'^2}}$, the results of the hot-wire measurement are slightly higher than those of the DNS. The result obtained with SPIV ($\mathrm{Re}_\theta = 7800$) is between both, but closer to the HWA. The differences with DNS are attributed to the low Reynolds number influence. However, when it is very close to the wall, the difference of $\sqrt{\overline{v'^2}}$ or $\sqrt{\overline{w'^2}}$ between the results of SPIV

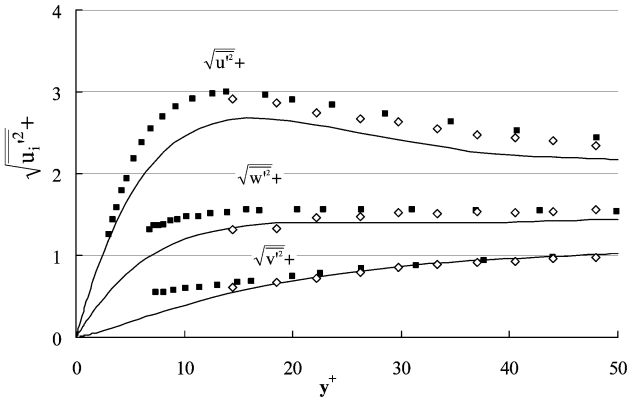

Fig. 14. Comparison of the profiles of fluctuations of SPIV (◊), hot-wire anemometry [15] (■) and DNS [22] (-)

and HWA increases. The main reason is that X-wire probes show an increasing bias when approaching the wall. This is due to wall interference and velocity gradients at the scale of the probe (0.5 mm). Considering this effect, the results reveal an excellent behavior of the SPIV measurement.

As is well known, Reynolds shear stress is a critical parameter of the turbulence. Figure 15 shows the data obtained by the two experimental methods (HWA and SPIV) compared with the results of DNS [22] and with the *Van Driest* model [20]. This model has been improved taking into account the weak pressure gradient of the test section $\partial p/\partial x = 0.057\,\mathrm{Pa/m}$ ($\partial p^+/\partial x^+ = 3.65 \times 10^{-4}$). The results of SPIV are similar to those of the Van Driest model and of the DNS. However, the results of HWA deviate considerably from the others, which once again shows the influences of the near-wall interference and gradients at the scale of the probe. This explains the low values of the turbulent shear stress of HWA. Small oscillations are visible in the PIV results due to the lack of convergence on this small term.

Figure 16 presents the comparison of spectra obtained from SPIV and from HWA using a local Taylor hypothesis [23]. In Fig. 16, $k_{\min}$ is the minimum wave number accessible with PIV ($k_{\min} = 2\pi/L_{\mathrm{f}}$, L_{f} being the field size) and k_{c} is the cutoff wave number of PIV due to the windowing effect (see [4]). According to *Foucaut* et al. [4], the PIV results are qualified to compare with the results of HWA only in the region between $k_{\min}$ and k_{c} (PIV cutoff wave number). In Fig. 16b, E_{33} shows a perfect fit with the result of the hot-wire anemometry. The E_{22} PIV spectrum (Fig. 16a) shows a slightly higher noise level than the E_{33} one at high wave number. This is probably due to the variation in magnification across the field and to the stretching effect in the x-direction linked to the stereoscopic setup. According to the experimental setup used, the w-component is always perpendicular to the axis of the lenses

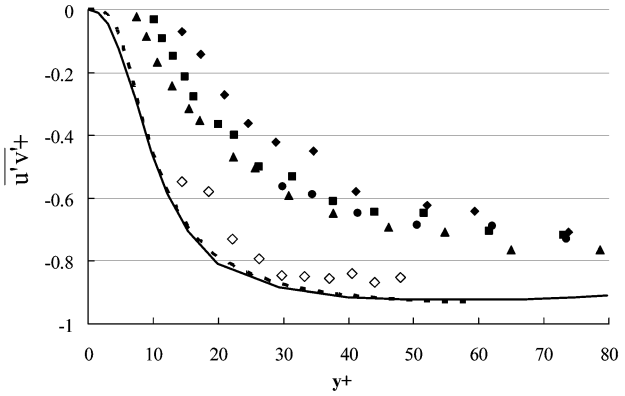

Fig. 15. Comparison of mean Reynolds shear stress of SPIV ($\mathrm{Re}_\theta = 11\,400$ (◊)), hot-wire anemometry [15] ($\mathrm{Re}_\theta = 11\,400$ (▲), 114 800 (■) and 20 600 (●)), Van Driest model [20] (...) and DNS [22] (-)

and is less affected than the v-component by the reconstruction process. The u-component (E_{11} spectrum not shown) is build from the same elements as v. It shows a similar behavior as E_{22} [24].

Figures 17a,b show the PDF of the v'- and w'-component, respectively. The PDF of w' shows much higher oscillation than that of v' (which is comparable to v'). As explained before, this is due to a peak-locking effect amplified by the gradient through the lightsheet. For v' (or u'), these oscillations are smoothed out by the stretching in the reconstruction procedure. Only a small difference in the height of the peak of v' is observable due to the noise caused by the strong velocity gradient near the wall. This difference disappears above the plane 4 (above this wall distance Fig. 10 shows that the gradient effect is negligible).

As is well known, the third-order moment of a random signal (e.g., signal A) S_A describes the asymmetry or skewness of the corresponding probability density function, while the fourth-order moment F_A (also referred to as flatness) reveals the frequency of occurrence of events far from the axis. These parameters are defined as:

$$S_\mathrm{A} = \frac{\overline{A^3}}{\overline{A^2}^{3/2}}\,,$$
$$F_\mathrm{A} = \frac{\overline{A^4}}{\overline{A^2}^2}\,. \tag{6}$$

For the skewness factor, $S_\mathrm{A} = 0$ is expected if the probability density function of A is symmetric. In turbulence, the three velocity fluctuations (u, v and w) often have a nearly Gaussian distribution. For such a distribution, $S_\mathrm{A} = 0$ and $F_A = 3$ are obtained.

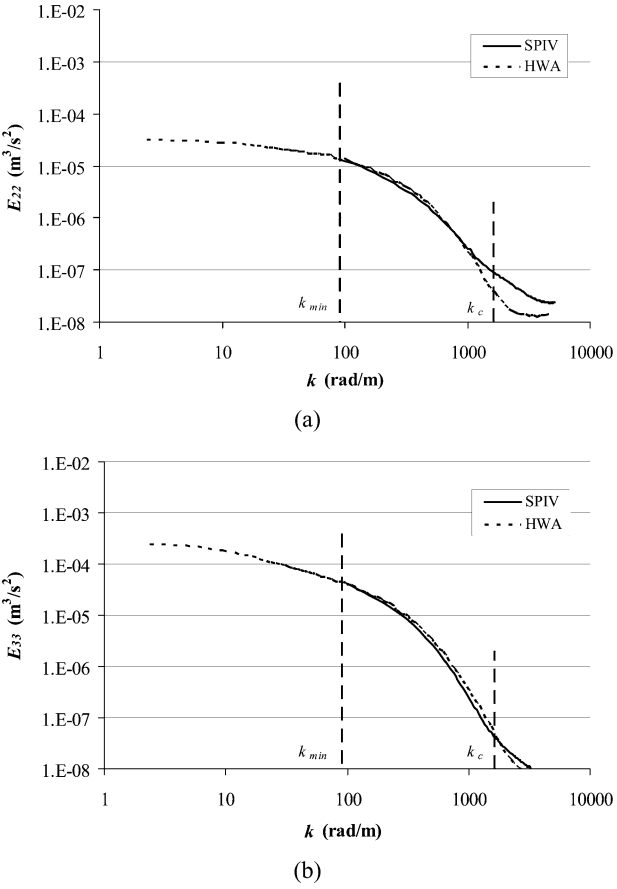

Fig. 16. Velocity spectrum of the v-(**a**) and w-(**b**) components of plane 4, comparison with HWA

Figures 18 to 20 show, respectively, the profiles of skewness factors $S_{u'}$, $S_{v'}$ and $S_{w'}$ for the three velocity fluctuations. In Fig. 18, the skewness factor for the streamwise fluctuations $S_{u'}$ is in very good agreement with the results of HWA [15]. For $S_{u'}$, both results indicate an increase toward the wall known to be due to the strong intermittency in the viscous sublayer. Above $y^+ \cong 15$, $S_{u'}$ is more or less constant and nearly zero, indicating a Gaussian behavior that is confirmed by the shape of the PDF. These results are in agreement with those of [25], who found that this location varies between $y^+ = 15$ and 20 for various Reynolds numbers. The positive value near the wall indicates that the frequency of occurrence of high positive streamwise fluctuations (high-speed streaks and sweeps) is higher than that of high negative fluctuations in this region.

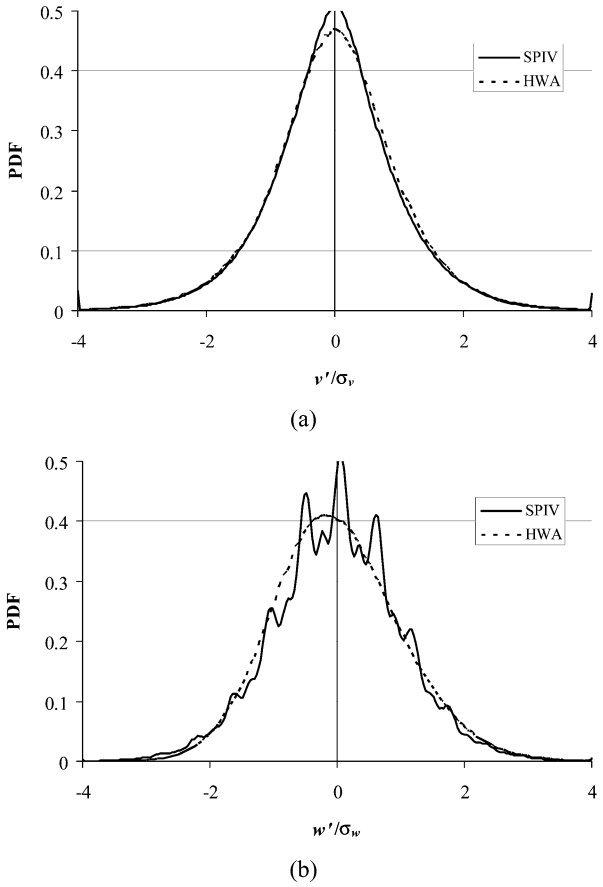

Fig. 17. PDF of the normalized fluctuations of the v-(**a**) and w-(**b**) components of plane 4, comparison with HWA

In Fig. 19, $S_{v'}$ agrees also very well with HWA. Again, it is nearly zero above $y^+ \cong 20$. The larger scatter compared to $S_{u'}$ is attributed to the small value of this component compared to u' (Fig. 14). The positive value of $S_{v'}$ evidences the asymmetry of the PDF close to the wall, indicating the predominance of ejections on the statistical behavior of this component.

The skewness factor $S_{w'}$ should be zero in a truly two-dimensional boundary layer due to the symmetry of the mean flow in the spanwise direction. This is confirmed by the present SPIV results in Fig. 20, where the factor $S_{w'}$ is nearly zero. The HWA results have a slightly positive value of about 0.25 that is comparable to that found by *Fernholz* and *Finley* [25]. It is attributed to a bias in the HWA measurements due either to a slight rotation

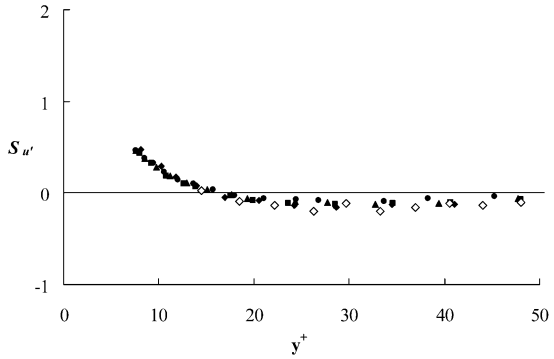

Fig. 18. Skewness factor $S_{u'}$. SPIV ($\mathrm{Re}_\theta = 7800$ (◊)), hot-wire anemometry [15] ($\mathrm{Re}_\theta = 11\,400$ (▲), $114\,800$ (■) and $20\,600$ (●))

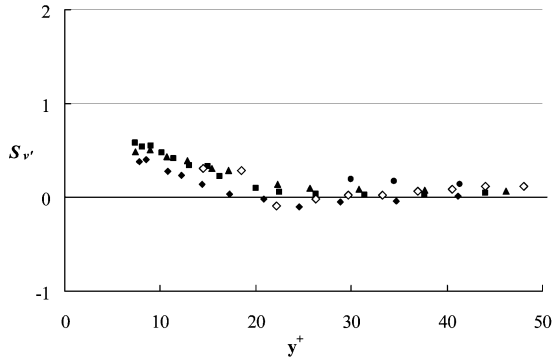

Fig. 19. Skewness factor $S_{v'}$. SPIV ($\mathrm{Re}_\theta = 7800$ (◊)), hot-wire anemometry [15] ($\mathrm{Re}_\theta = 11\,400$ (▲), $114\,800$ (■) and $20\,600$ (●))

of the probe around its axis or to the local velocity gradient at the scale of the probe.

Figures 21 to 23 show, respectively, the profiles of skewness factors $F_{u'}$, $F_{v'}$ and $F_{w'}$. Figure 21 compares the flatness factor $F_{u'}$ obtained in the present study with that obtained by HWA [15]. Again the SPIV results are in very good agreement with HWA. For $y^+ \geq 15$, the present SPIV results show that $F_{u'}$ increases slightly from 2.4 at $y^+ = 15$ to 2.8 at $y^+ = 39.7$ and then levels off afterwards. *Ueda and Hinze* [26] found a relationship between the position of the maximum of the streamwise normal Reynolds stress ($\overline{u'^2}$), the zero value of $S_{u'}$, and the minimum of $F_{u'}$. These characteristic points are at the same distance from the wall. In the present case, the maximum of ($\overline{u'^2}$) is at about $y^+ = 14$ (Fig. 14), the zero crossing of $S_{u'}$ is at around $y^+ = 16$

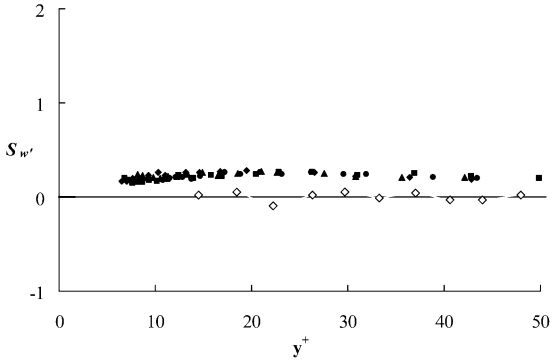

Fig. 20. Skewness factor $S_{w'}$. SPIV ($\mathrm{Re}_\theta = 7800$ (◊)), hot-wire anemometry [15] ($\mathrm{Re}_\theta = 11\,400$ (▲), $114\,800$ (■) and $20\,600$ (●))

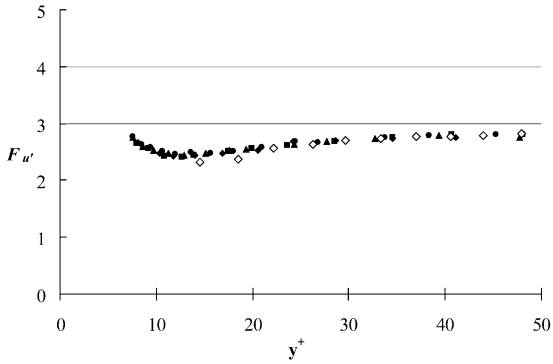

Fig. 21. Flatness factor $F_{u'}$. SPIV ($\mathrm{Re}_\theta = 7800$ (◊)), hot-wire anemometry [15] ($\mathrm{Re}_\theta = 11\,400$ (▲), $114\,800$ (■) and $20\,600$ (●))

in Fig. 18, and the minimum value of $F_{u'}$ is near to $y^+ = 12$. Considering the experimental errors involved, the results confirm the relationship obtained by [26]. Similar to $S_{u'}$, $F_{u'}$ is known to increase toward large positive values in the viscous sublayer ($y^+ \leq 5$) due to intermittency.

Figure 22 presents the flatness factor $F_{v'}$ compared with HWA. In SPIV, this parameter decreases sharply between $y^+ = 14.5$ and 22.2. When $y^+ > 22.2$, $F_{v'}$ decreases slowly with increasing wall distance and is in good agreement with the results of HWA for various Reynolds numbers. This result was also obtained by other researchers [22, 25, 27]. The large values at $y^+ = 14.5$ and 18.5 can be associated with the intermittent character of near-wall flow in the buffer layer. The differences with the results of HWA at $y^+ = 14.5$ and

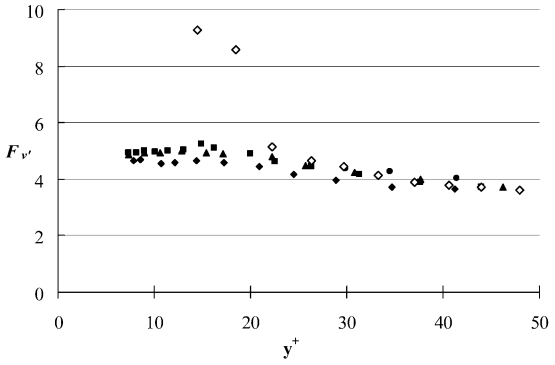

Fig. 22. Flatness factor $F_{v'}$. SPIV ($\mathrm{Re}_\theta = 7800$ (◊)), hot-wire anemometry [15] ($\mathrm{Re}_\theta = 11\,400$ (▲), $114\,800$ (■) and $20\,600$ (●))

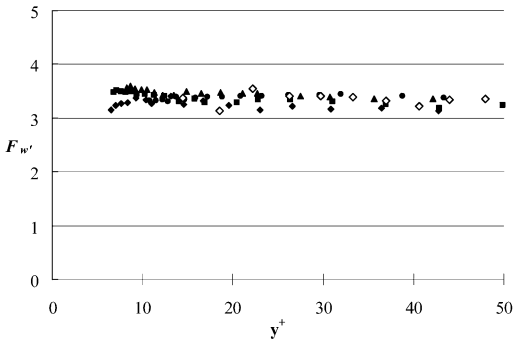

Fig. 23. Flatness factor $F_{w'}$. SPIV ($\mathrm{Re}_\theta = 7800$ (◊)), hot-wire anemometry [15] ($\mathrm{Re}_\theta = 11\,400$ (▲), $114\,800$ (■) and $20\,600$ (●))

18.5 are attributed to the velocity gradient at the size of the X-wire probe close to the wall.

Figure 23 compares $F_{w'}$ obtained by SPIV and HWA. There is a very good agreement. $F_{w'}$ is nearly constant. The value of 3.4 is the same as suggested by *Fernholz* and *Finley* [25].

7 Conclusions

In summary, an experiment of stereo-PIV was carried out to investigate near-wall turbulence. This experiment recorded 500 image pairs for each of 10 planes of a fully developed turbulent boundary layer flow along a flat plate. The first plane was placed at 14.5^+ from the wall. The spacing between neighboring planes was about 4^+. The Reynolds number based on the momentum

thickness Re_θ was 7800. Three methods are available to analyze the database, namely image mapping, vector warping and the Soloff technique. They were compared in order to select the most suitable method of analysis for our database. The comparison took into consideration different interpolation and shift methods. The whole comparison was based on the estimation of computation time, the estimation of accuracy, the spatial spectra and velocity PDFs. The results favored the Soloff method over all the others. For the Soloff method, the difference between Whittaker and integer shift PIV processing and the difference between using 3 and 5 calibration planes was negligible. As a result, the Soloff method with 3 calibration planes for projection and reconstruction, using integer shift for PIV analysis was chosen as the most suitable method for the database. The improvement provided by the correction process [10] was presented. Recently, *Calluaud* and *David* [28] and *Wieneke* [12] proposed a method based on the pinhole model. This model is based on previous work in the field of computer vision. It can incorporate some limited optical distortion and has the advantage of using less parameters in the least square fit than the Soloff method (24 instead of about 80). *Scarano* et al. [29] compared this method with the image warping method with misalignment correction. They found that the two methods are practically equivalent for a correctly aligned system. In the present study, the Soloff method was found to be the best compromise to analyze turbulent PIV data, but the differences from the other two methods (mapping and warping) were fairly limited. The main advantage for the moment of the Soloff method is its generality and overall accuracy and it seems that any reconstruction method, properly applied leads to errors smaller than the PIV processing errors.

Using this processing method, the whole database was analyzed. The results were presented in terms of the mean streamwise velocity, velocity fluctuations, Reynolds shear stresses,, the spectra and PDFs, and skewness and flatness. They were compared with those of hot-wire anemometry, DNS and the Van Driest model. The comparisons showed that the results of SPIV are in good accordance with those of other methods. In general, the results of SPIV are closer to those of the Van Driest model and DNS than to HWA in the very near wall region. This chapter concludes that SPIV is a suitable method to study near-wall turbulence.

References

[1] R. Adrian: Particle-imaging techniques for experimental fluid mechanics, Ann. Rev. Fluid Mech. **23**, 261–304 (1991) 191, 197

[2] J. Westerweel: Fundamentals of digital particle image velocimetry, Meas. Sci. Technol. **8**, 1379–1392 (1997) 191

[3] M. Raffel, M. Gharib, O. Ronneberger, J. Kompenhans: Feasibility study of three-dimensional PIV by correlating images of particles within parallel light sheets, Exp Fluids. **19**, 69–77 (1995) 191, 193

[4] J. Foucaut, J. Carlier, M. Stanislas: PIV optimization for the study of turbulent flow using spectral analysis, Meas. Sci. Technol. **15**, 1046–1058 (2004) 191, 201, 202, 212
[5] L. Lourenco: *Some Comments on Particle Image Displacement Velocimetry*, Von Karmann Institute for Fluid Dynamics, Lecture Series **1988-06** (Von Karmann Institute for Fluid Dynamics 1988) 191
[6] A. Prasad, R. Adrian: Stereoscopic particle image velocimetry applied to liquid flows, Exp. Fluids **15**, 49–60 (1993) 191, 192
[7] S. Soloff, R. Adrian, Z. Liu: Distortion compensation for generalized stereoscopic particle image velocimetry, Meas. Sci. Technol. **8**, 1441–1454 (1997) 192, 194, 196
[8] C. Willert: Stereoscopic digital particle image velocimetry for applications in wind tunnel flows, Meas. Sci. Technol. **8**, 1465–1479 (1997) 192, 193, 195, 196
[9] J. Westerweel, J. van Oord: Stereoscopic PIV measurements in a turbulent boundary layer, in *EUROPIV: Progress Towards Industrial Application* (Kluwer, Dordrecht 2000) pp. 459–478 192, 195
[10] S. Coudert, J. Schön: Back projection algorithm with misalignment corrections for 2D3C stereoscopic PIV, Meas. Sci. Technol. **12**, 1371–1381 (2001) 192, 196, 198, 208, 219
[11] N. Pérenne, J. Foucaut, J. Savatier: Study of the accuracy of different stereoscopic reconstruction algorithms, in M. Stanislas, J. Westerweel, J. Kompenhans (Eds.): *Proceeding of the EUROPIV 2 Workshop on Particle Image Velocimetry: Recent Improvements* (Springer, Berlin, Heidelberg 2004) pp. 375–390 192
[12] B. Wieneke: Stereo-PIV using self-calibration on particle images, Exp. Fluids **39**, 267–280 (2005) 192, 219
[13] R. Fei, W. Merzkirch: Investigations of the measurement accuracy of stereo particle image velocimetry, Exp. Fluids **37**, 559–565 (2004) 193, 208
[14] N. Lawson, J. Wu: Three-dimensional particle image velocimety experimental error analysis of digital angular stereoscopic system, Meas. Sci. Technol. **8**, 1455–1464 (1997) 196
[15] J. Carlier, M. Stanislas: Experimental study of eddy structures in a turbulent boundary layer using particle image velocimetry, J. Fluid Mech. **535**, 143–188 (2005) 196, 211, 212, 213, 214, 216, 217, 218
[16] T. Ursenbacher: *Traitement de vélocimétrie par images digitales de particules par une technique robuste de distortion d'images*, Ph.D. thesis, Ecole Polytechnique de Lausanne (2000) 198
[17] F. Scarano, R. Riethmuller: Advances in iterative multi-grid PIV image processing, Exp. Fluids **[Suppl.]**, S51–S60 (2000) 198
[18] J. Foucaut, B. Miliat, N. Pérenne, M. Stanislas: *Characterization of Different PIV Algorithms Using the EUROPIV Synthetic Image Generator and Real Images from a Turbulent Boundary Layer* (Springer, Berlin, Heidelberg 2004) 200, 201, 202, 204
[19] R. Keane, R. Adrian: Optimisation of particle image velocimeters-part I double pulsed systems, Meas. Sci. Technol. **1**, 1202–1215 (1990) 204
[20] E. R. van Driest: On turbulent flow near a wall, J. Aero. Sci. **23**, 1007–1011 (1956) 204, 212, 213

[21] C. Willert: Prososal for netCDF (re)implementation for use with planar velocimetry data, in M. Stanislas, J. Westerweel, J. Kompenhans (Eds.): *Proceeding of the EUROPIV 2 Workshop on Particle Image Velocimetry: Recent Improvements* (2004) pp. 251–262 210
[22] P. Spalart: Direct simulation of a turbulent boundary layer up to $\mathrm{Re}_\theta = 1410$, J. Fluid Mech. **1878**, 61–98 (1988) 211, 212, 213, 217
[23] J. O. Hinze: *Turbulence*, Series in Mechanical Engineering (McGraw-Hill 1975) 212
[24] C. Willert, M. Gharib: Digital particle image velocimetry, Exp. Fluids **10**, 181–193 (1991) 213
[25] H. Fernholz, P. Finley: The incompressible zero-pressure-gradient turbulent boundary layer: An assessment of the data, Prog. Aerospace Sci. **32**, 245–311 (1996) 214, 215, 217, 218
[26] H. Ueda, J. Hinze: Fine-structure turbulence in the wall region of a turbulent boundary layer, J. Fluid Mech. **61**, 125–143 (1975) 216, 217
[27] P. Vukoslavcevic, J. Wallace, J. Balint: The velocity and vorticity vector fields of a turbulent boundary layer, J. Fluid Mech. **228**, 25–51 (1991) 217
[28] D. Calluaud, L. David: 3D PIV measurements of the flow around a surface-mounted block, Exp. Fluids **36**, 53–61 (2004) 219
[29] F. Scarano, L. David, M. Bsibsi, D. Calluaud: S-PIV comparative assessment image dewarping+misalignment correction and pinhole+geometric back projection, Exp. Fluids **39**, 257–266 (2005) 219

Index